demonstrated how external heavy atoms can help to achieved long-lived RTP in many compounds. For example, introduction of halogen atoms (such as I or Br) generally enhances the PersL of metal-free organic systems [14, 98]. Hybrid perovskites, which are formed by combining organic and inorganic semiconductors at the molecular scale, exhibit high luminescence efficiency and carrier mobility and are emerging for potential optoelectronics applications. Yang et al. demonstrated that doping of fluorophores into hybrid perovskites can inhibit the T–T annihilation process, and thereby act as a promising strategy for designing highly efficient MPLMs [99]. Ema et al. demonstrated that strong PersL can be achieved through energy transfer to the T state in organic–inorganic hybrid quantum-well structure consisting of perovskite-type lead bromide well layers and naphthalene-linked ammonium barrier layers. More specifically, an efficient energy transfer occurs from the inorganic cations in the perovskite to the T state of the organic naphthalene derivative cations [100].

1.3.2.3 Inorganic–Organic Molecular Hybrid PLMs

This class of MPLMs are based on metal–organic frameworks (MOFs), which consist of networks of metal clusters or metal ions connected by organic ligands. As luminescent MOFs containing noble-metal and rare-earth elements such as Au, Pt, Ru, Ir, Tb, and Eu typically exhibit phosphorescence with lifetimes starting from microseconds to milliseconds, rational design of novel MOFs to obtain long-lived PersL is a challenging task [14]. The RTP exhibited in MOFs can be tuned by using different stackings of organic ligands and alternation of metal ions. For example, the phosphorescence lifetimes of the two different two-dimensional (2D) layered Cd-based MOFs [14], which were synthesized through a hydrothermal process and stabilized by both interlayer π–π and C–H$\cdots$π interactions, can be enhanced up to seconds by changing the stacking modes of the organic ligands and organic–metal coordination environment. Recently, various rare earth ion-containing MOFs such as Eu-MOFs and Tb-MOFs with long red and green phosphorescence lifetimes have been developed [93]. Moreover, it has been observed that the Cd-doped Ln-MOF systems such as Cd–Tb-MOF and Cd–Eu-MOF have longer lifetimes than the Eu/Tb-based MOFs. This is due to the RTP energy transfer from T_1 to a higher level of Tb^{3+} and Eu^{3+} as shown in Figure 1.8d. Furthermore, by comparing the energy levels of the lowest singlet excited state S_1 and the lowest triplet excited state T_1 with the higher energy level of Tb^{3+} and Eu^{3+} ions, it can find why Tb^{3+} is better than Eu^{3+} in terms of sensitization with higher energy transfer efficiency and a longer lifetime [101].

1.4 Synthesis Methods for IPLMs

Except additional traps required for the presence of PersL phenomenon, IPLM matrices are the same as those non-IPLMs. Therefore, typically similar methods are used to prepare IPLMs with only slight change of synthesis conditions so that efficient traps are formed. Figure 1.9 gives a pictorial representation of various

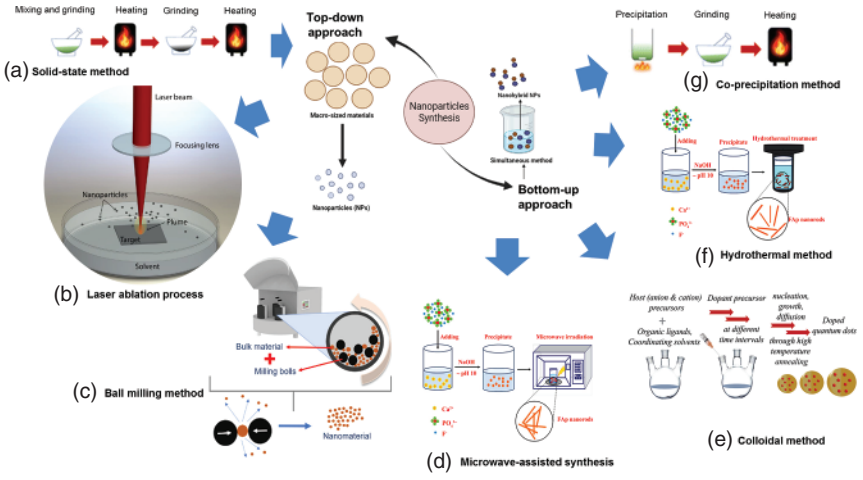

Figure 1.9 Pictorial representation of various top-down and bottom-up synthesis methods. Source: Adapted from Mujahid et al. [102] (a) solid-state method. Source: Adapted from Price et al. [103], (b) laser ablation process. Source: Adapted from Fernández-Arias et al. [104], (c) ball milling method. Source: Adapted from Barizão et al. [105], (d) microwave-assisted synthesis. Source: Adapted from Girija et al. [106], (e) colloidal method. Source: Adapted from Makkara and Viswanatha [107], (f) hydrothermal method. Source: Adapted from Duraisamy et al. [108], and (g) coprecipitation method. Source: Adapted from Price et al. [103].

synthesis methods for IPLMs, which are discussed elaborately below, while the synthesis of MPLMs will be discussed in Chapter 10.

1.4.1 Solid-State Method

The most widely usedmethod for synthesizing IPLMs is solid-state reactions at high temperatures owing to the advantage of simplicity and the ease of changing synthesis conditions. At first, solid precursors are mixed in required stoichiometric ratios and then intimately ground to maximize the contact between the precursors' particles. The mixed and ground precursors are then placed inside a tube or muffle furnace and heated up to a temperature that is sufficient to induce solid-state reactions but below the melting temperature of final IPLM compounds. Since heating close to or 200–300 °C below the melting temperature always leads to a dense, strongly agglomerated, and large grain size of final IPLM compounds, a postsynthesis grinding either manually or by using a ball mill is required for their practical applications as IPLMs. Choosing right temperatures for heating, which are sufficient for solid-state reactions and crystallization but do not lead to excessive sintering is therefore essential. Even if the final IPLM compounds become partly agglomerated, they can be separated using mild grinding. On the other hand, sintering might be advantageous as it may help get pore-free ceramics and thereby make IPLMs highly efficient because a large volume of scatter-free IPLM samples would be excited [109].

There are many examples where fluxes are also used in solid-state reactions of IPLMs, that is, inorganic salts such as chlorides and fluorides melt in between

precursor particles and facilitate their easier interdiffusion [110, 111]. Generally, the inorganic salts do not take part in the solid-state reactions of IPLMs; however, there are a few reported cases wherein fluxes get partly incorporated into the IPLM products and changed their PersL characteristics [112]. For example, when boric acid is used as the flux to prepare $SrAl_2O_4:Eu^{2+},Dy^{3+}$, boron creates mainly F-center related deeper traps and get stabilized by the incorporated B atom [113].

While heating time and temperature have a high impact on the performance of IPLMs, the heating atmosphere also can significantly influence their PersL properties. For example, if Eu^{2+} is the preferred valence state in a PLM, then it is essential to perform the thermal treatment in a reducing atmosphere. Otherwise, there is a high chance that Eu^{2+} can be oxidized to Eu^{3+} when heated in air, which leads to different PersL characteristics [114]. Similarly, for sulfides-based PLMs, synthesis in H_2S atmosphere is typically required. These atmospheric conditions can influence the trap density and characteristics, which are mostly related to various intrinsic defects such as oxygen or sulfur vacancies.

1.4.2 Ball Milling Method

Although solid-state reactions become the benchmark method for the synthesis of IPLMs with optimum performance, this method yields particles in the micrometer range in most cases. This limits the application of IPLM products in many areas, for instance, bio-imaging applications require the particle size of IPLMs in the nanometer range rather than the micrometer range. In such case, solid-state reaction method does not fulfill the requirement unless there is an effective way to decrease the particle size of IPLMs to the nanometer level. Ball milling is a top-down approach to reduce the particle size of IPLMs by mechanical impact and friction using planetary ball milling. Like manual grinding using a mortar and pestle, ball milling is also highly dependent on the size and hardness of starting IPLM materials. In many cases, a wide range of particle sizes of IPLM products are achieved. To get monodispersed particles, some kind of size selection is required. In the meantime, it has been observed that strong milling is detrimental to the PersL properties of IPLMs as it is difficult to avoid amorphization of their host matrices and oxidation of dopants due to surface exposure [115]. A postmilling thermal "healing" treatment at optimum temperatures that avoid particle growth and sintering can remove some of the side effects of ball milling.

1.4.3 Pulsed Laser Ablation Method

Pulsed laser ablation is another top-down method to reduce the size of bulk targets to nanoscale with the same chemical composition. In general, a pulse laser such as pulsed Nd:YAG laser of 1064 nm at 10 Hz can deliver a large amount of energy to the surface of targets like $SrAl_2O_4:Eu^{2+},Dy^{3+}$ pellet in acetone or ethanol. This creates a high impact pressure on the surface of $SrAl_2O_4:Eu^{2+},Dy^{3+}$ pellet to produce $SrAl_2O_4:Eu^{2+},Dy^{3+}$ NPs of ~7.5 nm with a narrow size distribution. This low-cost top-down method has already been used to produce IPLM nanoparticles (NPs) [116].

It is also possible to control the morphology of the IPLM NPs by properly adjusting pulse energy, laser wavelength, pulse frequency, and pulse width.

1.4.4 Solution-Based Methods

To overcome the limitation of solid-state reactions like difficult controlling particle size, morphology and dispersion of IPLMs, bottom-up synthesis can easily prepare PersL nanophosphors. Various solution-based methods including hydrothermal synthesis, sol-gel synthesis, colloidal synthesis, and coprecipitation always make nanosized particles with excellent morphology and size distribution. Unlike solid-state method wherein precursors need to react by solid diffusion, the solution-based methods involve intimate mixing of precursors on a molecular level. The particle size of the final IPLM products can be controlled by changing various synthetic conditions, such as pH, reaction temperature and time, precursor concentrations, and so on. Many IPLMs prepared by solution-based methods need postannealing treatment, which is often considered as a prerequisite to get sufficient PersL. On the other hand, annealing-free nanophosphors are flexible for surface functionalization when used for biological applications. Therefore, many new approaches to synthesize efficient PersL nanomaterials are emerging [117]. To get satisfactory PersL results, some specific methods have been developed for postannealing of preformed IPLM NPs while avoiding grain growth during thermal annealing. For example, by temporarily or permanently embedding IPLM NPs in a silica matrix as a template, the thermal annealing process can be performed [118]. Recently, we have developed a molten salt postannealing process to prepare monodispersed and bright PersL $ZnGa_2O_4:Cr^{3+}$ NPs with minimal agglomeration. It was demonstrated that mixing PersL NPs with molten salts can ensure good spatial isolation between adjacent nanomaterials during annealing, resulting in significantly enhanced luminescence with well-preserved morphology [119]. The solution-based synthesis methods are described below.

1.4.4.1 Hydrothermal Method

Among the solutions-based methods, hydrothermal method is one of the most widely used synthesis approach for preparing a variety of luminescence nanomaterials with controlled size and morphology. The luminescence nanomaterials can be prepared in a wide temperature range. This method possesses several advantages over the others, such as it can generate nanomaterials that are not stable at elevated temperature. Further, the morphology of the materials can be controlled by varying the synthesis parameters such as low-pressure or high-pressure conditions depending on the vapor pressure of the main composition in the reaction. In many cases of the synthesis of IPLMs, a post-heat treatment is necessary to generate PersL [120]. There are many reports that PersL can be improved by fine-tuning their nucleation kinetics and crystal size through controlled urea precipitation, and adjusting the Zn/Ga precursor ratio, and addition of ammonium nitrate, such as for hydrothermally synthesized ZnGa2O4:Cr^{3+} NPs [121].

1.4.4.2 Coprecipitation Method

Coprecipitation and thermal decomposition are common approaches for synthesizing metal oxide and fluoride NPs. For example, PersL nanophosphors of yttrium–aluminum–gallium garnet (YAGG) co-doped with Ce^{3+}, Cr^{3+}, and Pr^{3+} with various sizes were obtained by coprecipitation method followed by annealing at different temperature. It was observed that YAGG nanophosphor annealed at 1100 °C showing an acceptable degree of particle agglomeration and suitable for practical applications [122]. Likewise, $CaTiO_3:Pr^{3+}$ nanoparticles showing PersL characteristics with sizes ranging from 6 to 95 nm were prepared by a coprecipitation technique. Maximum phosphorescence occurred with increasing annealing temperature at 700 °C. The enhancement of PersL characteristics with increasing annealing temperature was due to a reduced surface-to-volume ratio, which decreased the surface defects acting as nonradiative recombination centers and increased the $^1D_2$–$^3H_4$ emission efficiency [123].

1.4.4.3 Colloidal Method

Among the bottom-up approaches, colloidal synthesis of PersL NPs was found to be more efficient in controlling the size, morphology, heterostructures, and optical properties of PersL NPs. For example, uniform X-ray-excitable PersL $Na(Gd,Lu)F_4:Ln^{3+}$ (Ln = Ce, Eu, Tb) NPs were first reported to be synthesized using this method by Cooper et al. in 2018 [39]. The method involves high-temperature coprecipitation of lanthanide fluoride using a noncoordinating solvent 1-octadecene (as the primary solvent) in combination with oleic acid (as a passivating ligand to prevent agglomeration) to direct nanoparticle growth. This method yields PersL NPs with very narrow size distributions and uniform morphology. The colloidal synthesis can also produce PersL heterostructured core-shell NPs. For example, CaF_2:Dy PersL NPs can be obtained through the colloidal synthesis method involving thermolysis of calcium trifluoroacetate in a fine-controllable manner. Furthermore, PersL heterostructured core–shell CaF_2:Dy@$NaYF_4$ NPs can be constructed in a controllable manner through this method due to excellent compatibility of CaF_2 crystal lattice with cubic phase $NaYF_4$ [21].

1.4.4.4 Template Method

Another accurate way to control the size and morphology of IPLM NPs is to use a template such as textured substrate or 3D porous structure to prepare them. For example, mesoporous silica nanospheres have been widely used to prepare various monodispersed IPLM NPs with well-preserved morphology such as SiO_2@$SrMgSi_2O_6:Eu^{2+},Dy^{3+}$ and SiO_2@$ZnGa_2O_4:Cr^{3+}$ [124, 125].

1.4.4.5 Other Methods

Apart from the synthesis methods described above, there are many other solution-based methods available for synthesizing IPLMs, wherein the high temperature required for solid-state reaction or precursor decomposition can be avoided if liquid precursors are used in a solvothermal or hydrothermal process, or in a microwave-assisted synthesis. Combustion synthesisis another method to

prepare IPLMs and their NPs, while the reactions may be very fast and sometimes hard-to-control. Despite many drawbacks, solid-state reactions are still the most widely employed method to prepare efficient IPLMs with desirable PersL performance. However, for bio-medical applications requiring monodispersed PLM NPs, bottom-up synthesis methods using liquid precursors are better suited. So far, the challenge to balance the small particle size and PersL intensity of IPLMs still remains a main issue.

1.4.5 PersL Glass, Glass Ceramics and Composites

Most of IPLMs prepared by the aforementioned methods are in powder form. However, for practical application such as in emergency signaling like the exit and fire extinguisher boards, they require additional processing to enable maneuvering and device project. One strategy is to employ functional composites by dispersing IPLMs powders homogeneously in polymer hosts like poly(methyl methacrylate) (PMMA). Although PMMA is able to keep a good percentual of its optical transparency, it undergoes several mechanical damages due to long exposure to UV light, which are difficult to restore with any treatment.

On the other hand, glasses such as phosphate and fluorophosphate glasses possess good resistance to high-energy radiation exposure and even though some defects are generated due to long exposure to high-energy radiation. Such defects can be easily healed after a thermal treatment. Moreover, phosphate glasses possess high chemical, thermal, and mechanical stability in addition to having extensive optical transmission in the wide UV to near-infrared spectrum region. Therefore phosphor-in-glass (PiG) composites make good alternatives to PMMA composites. The ILPMs can be embedded into glass hosts by their direct doping into them using melting-quenching technique, also known as "frozen sorbet method." For example, PersL $Sr_2MgSi_2O_7:Eu^{2+},Dy^{3+}$ (SMSO) polycrystalline material was embedded into the $80NaPO_3–20Ga_2O_3$ compositional glass system. Source: Adapted from Merízio et al. [126].

1.5 Measurements and Characteristics of PersL

The three major factors that regulate PersL output are the excitation, emission, and duration of PersL. While the PersL emission profile and decay profile can be measured using a convention emission spectroscopy after ceasing the excitation, the measurement of PersL excitation is a much more difficult process to detect and grasp. This is because of the fact that if someone measures PersL excitation spectrum in conventional excitation spectroscopy, then it is not certain whether the spectrum is originating due to excitation of PersL or only that of conventional luminescence. Furthermore, a strong PersL will make the conventional luminescence spectrum flattened down because of high background and low signal-to-noise ratio. Below we have discussed the measurement of the PersL excitation and emission for PLMs and their characteristics.

1.5.1 Excitation and Emission Characteristics

Many PLMs are often charged using UV or visible light with energies lower than the band gap energy of host matrices. However, when ionizing radiation such as X-rays is used, it is possible to fill different traps simultaneously unlike optical charging. This is attributed to the creation of an avalanche of delocalized electron–hole pairs by the high-energy X-rays. On the other hand, optical charging occurs through direct excitation of activators or through band-to-band excitation. Figure 1.10a shows the charging process followed by the decay profiles of $CaS:Eu^{2+},Dy^{3+}$ phosphor. The charging was carried out with 456 nm of excitation wavelength,

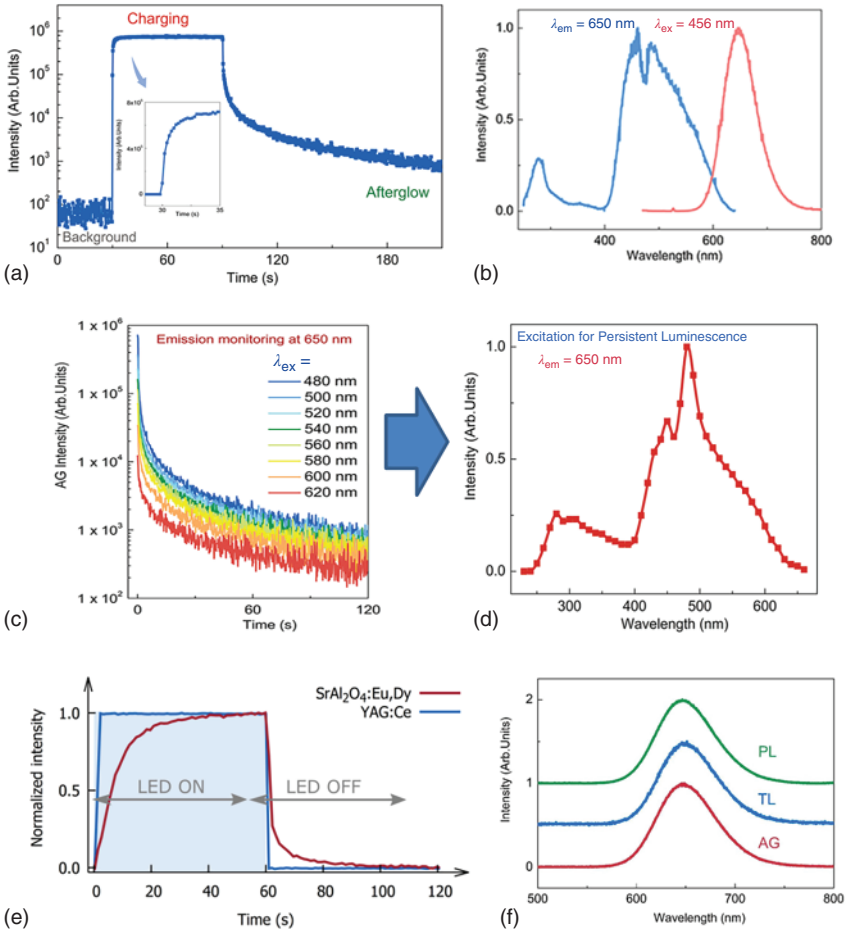

Figure 1.10 (a) Charging and afterglow decay profiles of $CaS:Eu^{2+},Dy^{3+}$ phosphor with 650 nm as the monitoring emission wavelength. Inset shows the starting points of the charging process. (b) PL excitation and emission spectra. (c) PersL decay profile at various excitation wavelengths of and the emission wavelength of 650 nm. (d) PersL excitation spectrum. Source: Adapted from Du and Poelman [127]. (e) Comparison of charging and decay profiles of a normal $Y_3Al_5O_{12}:Ce^{3+}$ phosphor and the benchmark PLM of $SrAl_2O_4$:Eu,Dy. Source: Adapted from Heggen et al. [128]. (f) Comparison of PersL (or afterglow, AG) and TL of $CaS:Eu^{2+},Dy^{3+}$. Source: Adapted from Du and Poelman [127].

whereas the light emission during charging and afterglow was monitored at 650 nm according to excitation and emission maxima of the photoluminescence (PL) given in Figure 1.10b. As shown in the inset of Figure 1.10a, the initial enhancement of light emission intensity originates due to combination of steady-state PL and afterglow emission of CaS:Eu^{2+},Dy^{3+}. During this time interval some of the excited electrons are getting stored in the traps while the others are coming back to the ground state of the activators and resulting PL. Due to continuous excitation process, when the rates of trapping and detrapping of the charge carriers are the same, a steady state with stable light output is achieved and resulting a flat line in charging spectra. When the excitation source is ceased, it will generate afterglow as shown in the decay profile. During this time, only the detrapping process occurs. However, the PL excitation maxima are not always the most efficient charging wavelength. One needs to measure the PersL excitation spectra for that. This can be done by measuring the decay profile at various wavelengths of excitation. For example, the decay profiles of CaS:Eu^{2+},Dy^{3+} can be monitored at 650 nm after one-minute excitation with monochromatic light starting from 230 to 660 nm with an interval of 10 nm. The PersL excitation spectrum can then be constructed by plotting the intensity at 650 nm as a function of the excitation wavelength. Figure 1.10c shows the PersL decay profiles at various excitation wavelengths, while Figure 1.10d shows the PersL excitation spectra at 650 nm wavelength of emission. The PersL excitation spectrum shows that the most efficient charging wavelength for this ILPM is ~480 nm.

Thus, PersL excitation spectra (or trap-filling spectra) generally provide the chargeable wavelength range of PLMs. One major difference between PL and PersL excitation processes of a PLM is that PL excitation spectra can be generated by using low energy light as excitation source (e.g. red light as excitation source for NIR PLMs), but in most cases, low energy light would not be able to charge the traps effectively for PersL, which rather requires higher energy photons. For example, although $LiGa_5O_8$:Cr^{3+} shows three different broad excitation bands in the UV, blue, and red regions for PL, only UV band can efficiently charge its traps and subsequently generate PersL [129]. Figure 1.10e shows the comparison of charging and decay profiles of a normal $Y_3Al_5O_{12}$:Ce^{3+} phosphor and the benchmark PLM of $SrAl_2O_4$:Eu,Dy. As discussed earlier, the light output in the case of PLMs, PersL intensity increases to the maximum only after a sufficiently long illumination time, a dynamic equilibrium of trap filling by the illumination and emptying traps by the room temperature thermal energy, or by optically stimulated luminescence using the same source. Since there are no tarps in the normal phosphors, their light output reaches the maximum immediately once the charging process is initiated. On the other hand, since the normal phosphor does not show any PersL and having a very fast decay, its light output intensity immediately comes down to zero as the excitation source is turned off. In contrast, a PLM keeps on emitting light after ceasing the excitation source. Figure 1.10f showed the comparison of emission spectra generated due to PL, PersL (or afterglow) and TL of CaS:Eu^{2+},Dy^{3+}. It was observed that the PersL and TL spectra are very similar to the steady-state PL. This suggests that all emissions originate from the same activator, that is, Eu^{2+} ions.

1.5.2 Trap Properties

1.5.2.1 Trap Depth and Optimum Temperature for Potential Applications

It is now well understood that the deeper the trap depth and the higher the energy barrier, the more heat is required to release the charge carriers from the traps of PLMs. The shallow traps, which are very close to CB or VB, are emptied very fast at room temperature. In contrast, deep traps are rarely emptied at room temperature and show PersL only at elevated temperatures. Therefore, temperature-dependent PersL of PLMs is largely determined by the trap depth profile of existing traps and their possible distribution in the host matrices. Trap depth is generally determined by TL experiment which is based on the emission read-out of a preirradiated IPLM sample caused by the constant heating wherein the thermal energy liberates the excited charge carriers from the traps. As shown in Figure 1.11a, TL glow curves can be obtained by plotting TL emission intensity (I) versus heating temperature (T). The various peaks in the glow curves reveal the existence of various traps at their corresponding thermal energy or trap depths (shallow or deep), which are responsible for PersL. Therefore, trap depths can be evaluated via the initial rise analysis of glow curves. As shown in Figure 1.11a, the deep traps are appeared at higher temperature in the TL glow curve, which is due to their higher tarp depth. In other words, higher thermal energy is required to release the charge carriers from deep traps.

The temperature dependent PersL characteristic of a PLM determines its application eligibility in various environmental conditions. This has led to the concept of the optimum working temperature, $T_{optimum}$ at which the maximum PersL output of a PLM is achieved within a reasonable time frame [130]. It has been observed that most commercial ILPMs have $T_{optimum}$ at around room temperature, which ensures a large number of room-temperature applications like emergency lighting, decoration, safety signage, and night-vision surveillance. The $T_{optimum}$ can be determined by the difference between two TL read-out events (TL_1–TL_2), with and without fading, as a function of ambient temperature. For example, Figure 1.11b,c represents the TL glow curves of IPLM of CaS:Eu^{2+},Dy^{3+} without fading and with 30 minutes of fading between irradiation and heating stage. While the PersL decay profiles at various temperature in Figure 1.11d show optimum performance around −20 °C, the $T_{optimum}$ is also found to be at a low temperature range, around −20 °C as shown in Figure 1.11e. This suggests that this PLM is more suited for low-temperature operation. Therefore, researchers need to focus on the trap depth engineered of PLMs carefully before designing them for particular applications at a certain temperature range.

1.5.2.2 Controlling Trap Filling and Releasing Kinetics by Temperature and Pump Power

Both trap filling and releasing processes by charge carriers co-exist in PLMs during the charging process. Owing to their low thermal barrier, shallow traps are much more easily depopulated than deep traps. Thus, the occupancy of traps can be varied by performing charging process at different temperatures. For example, at a low temperature which is above the thermal barrier, both shallow and deep

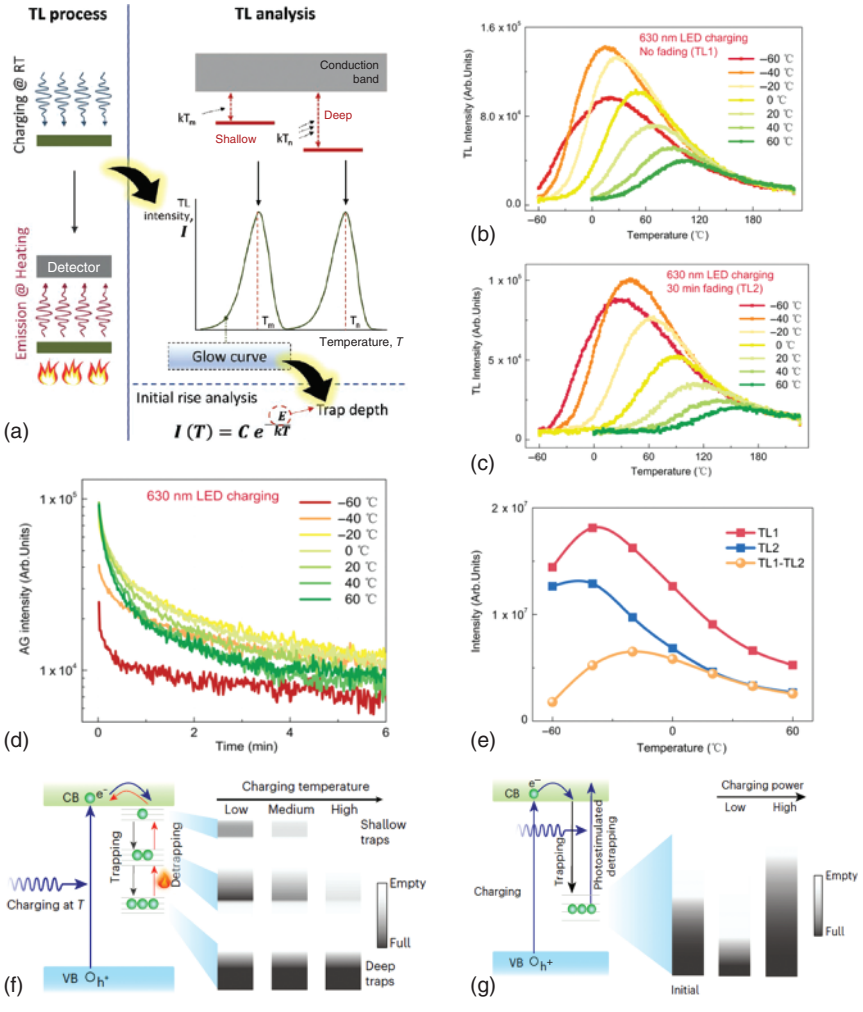

Figure 1.11 (a) Pictorial representation of trap depth's analysis through TL measurement and TL study. TL measurement can be carried out after charging IPLMs at room temperature followed by monitoring the emission upon continuous heating. Source: Adapted from Wang and Mao [46]. TL glow curves of PersL CaS:Eu^{2+},Dy^{3+} phosphor: (b) without fading and (c) with 30 minutes fading between irradiation and heating stage. (d) PersL decay profiles at various temperatures. (e) Measurement of $T_{optimum}$. Source: Adapted from Du and Poelman [127]. Control of trap filling by manipulation of (f) charge temperature T and (g) power density, respectively. Source: Adapted from Liang et al. [29]/Springer Nature.

traps can be filled. However, as the temperature is increased, the charge carriers in shallow traps become unstable against strong thermal stimulation. In contrast, the charge carriers in deep traps are stable. They become unstable only at very high temperature, that is, until the thermal stimulation matches their thermal barrier (Figure 1.11f). Therefore, due to the well-preserved characteristics of shallow traps at low temperature, slightly higher PersL can be achieved when PLMs are charged

at low temperature instead of high temperature, which results in depletion of both shallow and intermediate traps.

At a particular excitation wavelength, TL spectra of PLMs do not vary appreciably by changing the excitation's power, suggesting a constant occupation of different traps for particular excitation energy. However, if different excitation sources are used, then different occupancy of traps is observed for a particular PLM due to their different trap filling and de-trapping capabilities. For instance, when $LaMgGa_{11}O_{19}:Cr^{3+}$ is charged using a 450 nm blue LED, its trapped charge carriers can partially escape from the traps by absorbing the same 450 nm excitation photons, which results in photo-induced trap depletion [131]. Since the de-trapping process outperforms the trapping process at low-power pumping, pumping at high power is required so that trapping rate can exceed the release rate and a saturation of charge carriers is achieved in order to generate intense and long-lasting PersL (Figure 1.11g).

1.5.2.3 PersL Lifetime and Storage Capacity

Usually, the performance of a PLM is evaluated by measuring the time dependency of PersL intensity following the irradiation of the PLM using a standard light source for a certain time. Since visible and NIR lights have different eye sensitivity, the units used to report these PersL curves are different. The PersL curves of visible PLMs are usually expressed in photometric units. However, since the emission spectra of NIR PLMs fall outside the spectral range of the eye sensitivity, the units are expressed in radiometric units. The surface luminance for visible PLMs is specified in the photometric luminance as cd/m^2, while the radiometric equivalent of the photometric luminance is used for UV and NIR PLMs as $mW/m^2/sr$. The "PersL lifetime" is the time when a benchmark luminance of $0.32\,mcd/m^2$ is reached since the ceasing of the excitation source. In the PersL field, another benchmark luminance value of $0.30\,mcd/m^2$ is also often used. The storage capacity of a PLM is expressed as the number of photons emitted by one gram of phosphor during the phosphor's afterglow. This metric allows comparing storage capacity of PLMs independent of their spectral characteristics and morphology. For example, the storage capacity of the benchmark $SrAl_2O_4$:Eu,Dy PLM has been determined to $(1.57 \pm 0.03) \times 10^{17}$ photons/gram which is equal to ~1.6% of the Eu activators being ionized. This indicates that there is still needed improvement for this benchmark PLM [132]. The storage capacity can be measured in a fairly straightforward way. At first, PLMs are incorporated into a transparent polymer in order to excite all the PLM particles uniformly. Next, the PLMs are excited until saturation, or dynamic equilibrium is reached. Once the charging process is completed and the excitation source is turned off, the PersL curve of the PLM-containing polymer layer is started recording using a calibrated radiometric or photometric detector. As discussed earlier, PersL performance depends on the type of excitation sources being used and UV sources are more effective to fill all traps than visible and NIR sources. Therefore, it is necessary to mention the excitation source, its intensity, and the

spectral output, or more specifically, the parameters that are chosen to mimic the intended application for certain types of PLMs.

1.5.3 Trap Manipulation

As discussed earlier, trap manipulation holds the key for successful development of efficient PLMs and traps are created by various intrinsic lattice point defects, including vacancy and antisite defects, or impurity defects. In many cases, multiple-point defects can co-exist in matrices and create various types of traps with different trap depth profiles. Depending on trap depth or thermal barrier, some traps are involved in the trapping process of charge carriers while others are not. Vacancies such as cation and anion vacancies are created due to charge imbalance in matrices. These vacancies are often created simultaneously during the material synthesis of PLMs in equal numbers to maintain charge neutrality and are known as Schottky defects. Aliovalent substitution, that is, substituting lattice ions with ions of different valence, may create both positively and negatively charged defects. For example, doping Ge^{4+} and Mn^{4+} at Al^{3+} site in $LaAlO_3$ creates NIR PersL lasting for more than 20 hours due to the creation of both positively and negatively charged vacancies along with interstitial defects [133]. Similarly, nonstoichiometric synthesis of PLMs wherein the ionic stoichiometry of precursors is slightly changed before the synthesis generated Zn vacancies in $Zn_{2.94}Ga_{1.96}Ge_2O_{10}:Cr^{3+},Pr^{3+}$ [134]. The negatively charged Zn vacancies acted as hole traps and significantly increased the intensity and duration of NIR PersL.

Co-doping lanthanides is the most widely used strategy to generate electron and hole traps. As discussed in the band-engineering model (Figure 1.5c), where divalent lanthanides like Pr^{2+}, Nd^{2+}, Dy^{2+}, and Tm^{2+} with their ground states positioned just below the CB within the host band gap, their trivalent lanthanides, that is, Pr^{3+}, Nd^{3+}, Dy^{3+}, and Tm^{3+}, can serve as electron acceptors. In contrast, since the energy gap between the CB and ground state of Sm^{2+} and Yb^{2+} is high, Sm^{3+} and Yb^{3+} generate deep traps.

Other successful strategies include changing the sintering atmosphere or irradiating PLMs with high-energy rays, which are successful in generating desired traps. For example, when $Ca_2SnO_4:Gd^{3+},Eu^{3+}$ is sintered in a nonoxidizing atmosphere, oxygen vacancies are generated to act as efficient electron traps and yield much longer PersL than that sintered in air. Similarly, NIR PersL from $CaTiO_3:Cr^{3+}$ can only be generated when it is prepared in a reducing atmosphere to create oxygen vacancies [135]. In many cases, when PLMs are irradiated with high-energy photons, small anions can get displaced into interstitial sites, which create Frenkel defects acting as traps. For example, X-rays irradiation of lanthanide-doped fluorides can trigger hour-long PersL, which is attributed to the formation of fluoride vacancies acting as electron traps. High-momentum X-ray photons displace fluoride anions into interstitial sites during the elastic collisions [136]. Interestingly, when these X-ray irradiated PLMs are further heated

or irradiated with light, the displaced fluoride ions can diffuse back to their original sites and result in diminished PersL.

1.6 Summary and Challenges

In this introductory chapter of PersL, we have summarized the brief history of PLMs and their already established and possible future applications, various PersL mechanisms, fundamental understanding of various electron and hole traps, various types of PLMs and their synthesis procedures, and finally, some effective approaches to control traps to enhance the performance of PLMs. However, despite many substantial and rapid progresses in this class of emerging compounds, many challenges remain to be addressed for a clearer understanding before designing future PLMs. For example, defect centers within PLMs have both positive and negative impacts on their optical properties. In many cases, defect centers provide some nonradiative pathways to radiative centers, which thereby decrease the light yield of PLMs. Specifically, when the trap depth of defect-related traps is high, it will result in nonradiative transition to the VB instead of releasing the charge carrier to the CB (Figure 1.4c). Therefore, we must carefully avoid defects that provide nonradiative pathways. A thorough understanding of these defects or impurity-created energy levels inside the band gap of PLM host matrices is required before designing efficient PLMs. Furthermore, defects related traps should reproduce the PersL properties and should not disappear by changing atmospheric conditions.

Another major challenge of trap-controlled PLMs is the requirement of thorough characterization of these traps using multiple techniques. Multiple defects can exist in matrices and each of them can create separate traps. Therefore, the band-engineering model becomes more complex to understand. Since the energy position of point defects within the band gap of host matrices varies from one matrix to other, the trap depth of these defects also varies. Therefore, a similar defect, such as oxygen vacancy in oxide-based PLMs, may act as a shallow trap in one matrix but as a deep trap in another matrix due to the change of the band gap. Hence, it is difficult to construct a common band engineering model like that with the divalent and trivalent lanthanides. It is also essential to understand how the defects evolved in various matrices and the rate of capturing or releasing charge carriers from these trap states. A close collaboration between experimental and theoretical groups is required to understand the dynamic relationship between crystal structure, local electronic states, trap levels, and PersL properties.

References

1 Harvey, E.N. (1957). *A History of Luminescence from the Earliest Times Until 1900*. Philadelphia, PA: American Philosophical Society.
2 Yen, W.M. and Weber, M.J. (2004). *Inorganic Phosphors: Compositions, Preparation and Optical Properties*. Boca Raton, FL: CRC Press.
3 Yen, W.M., Shionoya, S., and Yamamoto, H. (2007). *Phosphor Handbook*, 2e. Boca Raton, FL: CRC Press.

4 Xu, J. and Tanabe, S. (2019). Persistent luminescence instead of phosphorescence: history, mechanism, and perspective. *J. Lumin.* 205: 581–620.

5 Yuan, L., Jin, Y., Su, Y. et al. (2020). Optically stimulated luminescence phosphors: principles, applications, and prospects. *Laser Photonics Rev.* 14 (12): 2000123.

6 Lastusaari, M., Laamanen, T., Malkamäki, M. et al. (2012). The bologna stone: history's first persistent luminescent material. *Eur. J. Mineral.* 24: 885.

7 Hoogenstraaten, W. and Klasens, H.A. (1953). Some properties of zinc sulfide activated with copper and cobalt. *J. Electrochem. Soc.* 100: 366.

8 Smet, P.F., Moreels, I., Hens, Z., and Poelman, D. (2010). Luminescence in sulfides: a rich history and a bright future. *Materials* 3: 2834.

9 Murayama, Y. (2006). *History of Persistent Phosphors in Japan*. Night-Vision Industry Association of Japan.

10 Matsuzawa, T., Aoki, Y., Takeuchi, N., and Murayama, Y. (1996). A new long phosphorescent phosphor with high brightness, $SrAl_2O_4$:Eu^{2+},Dy^{3+}. *J. Electrochem. Soc.* 143: 2670.

11 Smet, P.F., Botterman, J., Van Den Eeckhout, K. et al. (2014). Persistent luminescence in nitride and oxynitride phosphors: a review. *Opt. Mater.* 36: 1913.

12 Rojas-Hernandez, R.E., Rubio-Marcos, F., Rodriguez, M.Á., and Fernandez, J.F. (2018). Long lasting phosphors: $SrAl_2O_4$:Eu,Dy as the most studied material. *Renew. Sust. Energ. Rev.* 81: 2759.

13 Liu, Y., Li, C., Ren, Z. et al. (2018). All-organic thermally activated delayed fluorescence materials for organic light-emitting diodes. *Nat. Rev. Mater.* 3: 18020–18024.

14 Gao, R., Kodaimati, M.S., and Yan, D. (2021). Recent advances in persistent luminescence based on molecular hybrid materials. *Chem. Soc. Rev.* 50: 5564–5589.

15 Yang, Z., Mao, Z., Xie, Z. et al. (2017). Recent advances in organic thermally activated delayed fluorescence materials. *Chem. Soc. Rev.* 46: 915–1016.

16 Nemoto & Co., Ltd. (n.d.). Phosphorescent pigment. https://www.nemoto.co.jp/en/luminouspigment/ (accessed 27 November 2024).

17 Poelman, D., Van der Heggen, D., Du, J. et al. (2020). Persistent phosphors for the future: fit for the right application. *J. Appl. Phys.* 128: 240903.

18 Li, Y., Gecevicius, M., and Qiu, J. (2016). Long persistent phosphors—from fundamentals to applications. *Chem. Soc. Rev.* 45: 2090–2136.

19 Feng, A. and Smet, P.F. (2018). A review of mechanoluminescence in inorganic solids: compounds, mechanisms, models and applications. *Materials* 11 (4): 484.

20 Petit, R.R., Michels, S.E., Feng, A., and Smet, P.F. (2019). Adding memory to pressure-sensitive phosphors. *Light Sci. Appl.* 8 (1): 124.

21 Kersemans, M., Smet, P.F., Lammens, N. et al. (2015). Fast reconstruction of a bounded ultrasonic beam using acoustically induced piezo-luminescence. *Appl. Phys. Lett.* 107: 234102.

22 Pei, P., Chen, Y., Sun, C. et al. (2021). X-ray-activated persistent luminescence nanomaterials for NIR-II imaging. *Nat. Nanotechnol.* 16: 1011–1018.

23 Liang, L., Chen, N., Jia, Y. et al. (2019). Recent progress in engineering near-infrared persistent luminescence nanoprobes for time-resolved biosensing/bioimaging. *Nano Res.* 12 (6): 1279–1292.

24 Wu, S., Pan, Z., Chen, R., and Liu, X. (2017). *Long Afterglow Phosphorescent Materials*. Cham: Springer.

25 Xiong, P. and Peng, M. (2019). Recent advances in ultraviolet persistent phosphors. *Opt. Mater.: X* 2: 100022.

26 Zhou, Z., Li, Y., and Peng, M. (2020). Near-infrared persistent phosphors: Synthesis, design, and applications. *Chem. Eng. J.* 399: 125688.

27 Qiu, J., Li, Y., and Jia, Y. (2021). *Persistent Phosphors: From Fundamentals to Applications*. Woodhead Publishing.

28 Jin, H., Debroye, E., Keshavarz, M. et al. (2020). It's a trap! On the nature of localised states and charge trapping in lead halide perovskites. *Mater. Horiz.* 7: 397.

29 Liang, L., Chen, J., Shao, K. et al. (2023). Controlling persistent luminescence in nanocrystalline phosphors. *Nat. Mater.* 22: 289–304.

30 Dorenbos, P. (2005). Mechanism of persistent luminescence in Eu^{2+} and Dy^{3+} codoped aluminate and silicate compounds. *J. Electrochem. Soc.* 152: H107.

31 Ueda, J., Dorenbos, P., Bos, A.J.J. et al. (2015). Control of electron transfer between Ce^{3+} and Cr^{3+} in the $Y_3Al_{5-x}Ga_xO_{12}$ host via conduction band engineering. *J. Mater. Chem. C* 3: 5642.

32 Lyu, T. and Dorenbos, P. (2018). Charge carrier trapping processes in lanthanide doped $LaPO_4$, $GdPO_4$, YPO_4, and $LuPO_4$. *J. Mater. Chem. C* 6: 369.

33 Luo, H., Bos, A.J.J., and Dorenbos, P. (2016). Controlled electron–hole trapping and detrapping process in $GdAlO_3$ by valence band engineering. *J. Phys. Chem. C* 120: 5916.

34 Yamamoto, H. and Matsuzawa, T. (1997). Mechanism of long phosphorescence of $SrAl_2O_4$:Eu^{2+},Dy^{3+} and $CaAl_2O_4$:Eu^{2+},Nd^{3+}. *J. Lumin.* 72–74: 287–289.

35 Tanabe, S. and Hanada, T. (1996). Appearance of light-storage rare earth aluminate phosphors and their optical properties. *New Ceram.* 9: 27.

36 Takasaki, H., Tanabe, S., and Hanada, T. (1996). Long-lasting afterglow characteristics of Eu,Dy codoped SrO-Al_2O_3 phosphor. *J. Ceram. Soc. Jpn.* 104: 322.

37 Korthout, K., Van den Eeckhout, K., Botterman, J. et al. (2011). Luminescence and x-ray absorption measurements of persistent $SrAl_2O_4$:Eu,Dy powders: evidence for valence state changes. *Phys. Rev. B* 84: 085140.

38 Holsa, J., Aitasalo, T., Jungner, H. et al. (2004). Role of defect states in persistent luminescence materials. *J. Alloys Compd.* 374: 56–59.

39 Wang, L., Wang, C., Chen, Y. et al. (2022). Red-emitting $SrGa_2O_4$:Cu^{2+} phosphor with super-long persistent luminescence. *Chem. Mater.* 34: 10068–10076.

40 Zhuang, Y., Katayama, Y., Ueda, J., and Tanabe, S. (2014). A brief review on red to near-infrared persistent luminescence in transition-metal-activated phosphors. *Opt. Mater.* 36: 1907.

41 Katayama, Y., Kobayashi, H., and Tanabe, S. (2015). Deep-red persistent luminescence in Cr^{3+} doped $LaAlO_3$ perovskite phosphor for in vivo imaging. *Appl. Phys. Express* 8: 012102.

42 Liu, F., Yan, W., Chuang, Y.J. et al. (2013). Photostimulated near-infrared persistent luminescence as a new optical read-out from Cr^{3+}-doped $LiGa_5O_8$. *Sci. Rep.* 3: 1554.

43 Yang, T., Jiang, H., Hai, O. et al. (2021). Effect of oxygen vacancies on the persistent luminescence of $Y_3Al_2Ga_3O_{12}:Ce^{3+},Yb^{3+}$ phosphors. *Inorg. Chem.* 60 (23): 17797–17809.

44 Pan, Z., Lu, Y.Y., and Liu, F. (2012). Sunlight-activated long-persistent luminescence in the near-infrared from Cr^{3+}-doped zinc gallogermanates. *Nat. Mater.* 11: 58–63.

45 Clabau, F., Rocquefelte, X., Jobic, S. et al. (2005). Mechanism of phosphorescence appropriate for the long-lasting phosphors Eu^{2+}-doped $SrAl_2O_4$ with codopants Dy^{3+} and B^{3+}. *Chem. Mater.* 17: 3904–3912.

46 Wang, X. and Mao, Y. (2022). Emerging ultraviolet persistent luminescent materials. *Adv. Opt. Mater.* 10: 2201466.

47 Kang, F., Sun, G., Boutinaud, P. et al. (2021). Recent advances and prospects of persistent luminescent materials as inner secondary self-luminous light source for photocatalytic applications. *Chem. Eng. J.* 403: 126099.

48 Wang, X., Chen, Y., Liu, F. et al. (2020). Solar-blind ultraviolet-C persistent luminescence phosphors. *Nat. Commun.* 11: 2040.

49 Liu, Q., Feng, Z.Y., Li, H. et al. (2021). Non-rare-earth UVC persistent phosphors enabled by bismuth doping. *Adv. Opt. Mater.* 9: 2002065.

50 Wang, X., Chen, Y., Kner, P.A., and Pan, Z. (2021). Gd^{3+}-activated narrowband ultraviolet-B persistent luminescence through persistent energy transfer. *Dalton Trans.* 50: 3499.

51 Jin, Y.H., Hu, Y.H., Duan, H. et al. (2014). The long persistent luminescence properties of phosphors: Li_2ZnGeO_4 and $Li_2ZnGeO_4:Mn^{2+}$. *RSC Adv.* 4: 11360–11366.

52 Kitagawa, Y., Ueda, J., and Tanabe, S. (2022). Blue persistent phosphor of $YSiO_2N:Ce^{3+}$ developed by codoping Sm^{3+} or Tm^{3+} ions and thermoluminescence analysis of their trap distributions. *Phys. Status Solidi A* 219: 2100670.

53 Mei, Y., Xu, H., Zhang, J. et al. (2015). Design and spectral control of a novel ultraviolet emitting long lasting phosphor for assisting TiO_2 photocatalysis: $Zn_2SiO_4:Ga^{3+},Bi^{3+}$. *J. Alloys Compd.* 622: 908–912.

54 Wang, X. and Mao, Y. (2022). Recent advances in Pr^{3+}-activated persistent phosphors. *J. Mater. Chem. C* 10 (10): 3626–3646.

55 Yang, Y.M., Li, Z.Y., Zhang, J.Y. et al. (2018). X-ray-activated long persistent phosphors featuring strong UVC afterglow emissions. *Light Sci. Appl.* 7: 88.

56 Raeiszadeh, M. and Adeli, B. (2020). A critical review on ultraviolet disinfection systems against COVID-19 outbreak: applicability, validation, and safety considerations. *ACS Photonics* 7 (11): 2941–2951.

57 Yan, S., Liang, Y., Liu, J. et al. (2021). Development of ultraviolet-B long-lived persistent phosphors in Pr^{3+}-doped garnets. *J. Mater. Chem. C* 9: 14730.

58 Wang, X. and Mao, Y. (2021). Achieving ultraviolet C and ultraviolet B dual-band persistent luminescence by manipulating the garnet structure. *Adv. Opt. Mater.* 10 (5): 2102157.

59 Zhou, Z., Xiong, P., Liu, H., and Peng, M. (2020). Ultraviolet-A persistent luminescence of a Bi^{3+}-activated $LiScGeO_4$ material. *Inorg. Chem.* 59: 12920.

60 Sun, H., Gao, Q., Wang, A. et al. (2020). Ultraviolet-B persistent luminescence and thermoluminescence of bismuth ion doped garnet phosphors. *Opt. Mater. Express* 10: 1296.

61 Gutiérrez-Martín, F., Fernández-Martinez, F., Díaz, P. et al. (2010). Persistent UV phosphors for application in photo catalysis. *J. Alloys Compd.* 501: 193–197.

62 Sharma, S.K., Bettinelli, M., Carrasco, I. et al. (2019). Dynamics of charges in superlong blacklight-emitting CaB_2O_4:Ce^{3+} persistent phosphor. *J. Phys. Chem. C* 123: 14639.

63 Sonekar, R., Omanwar, S., Moharil, S. et al. (2009). Luminescence in $LaBaB_9O_{16}$ prepared by combustion synthesis. *J. Lumin.* 129: 624.

64 Yan, J., Ning, L., X., Huang, Y. C. et al. (2014). Luminescence and electronic properties of $Ba_2MgSi_2O_7$:Eu^{2+}: a combined experimental and hybrid density functional theory study. *J. Mater. Chem. C* 2: 8328–8332.

65 He, H., Fu, R.L., Song, X.F. et al. (2010). Observation of fluorescence and phosphorescence in $Ca_2MgSi_2O_7$:Eu^{2+},Dy^{3+} phosphors. *J. Electrochem. Soc.* 157: J69–J73.

66 Van den Eeckhout, K., Poelman, D., and Smet, P.F. (2013). Persistent luminescence in non-Eu^{2+}-doped compounds: a review. *Materials* 6: 2789–2818.

67 Takahashi, Y., Ando, M., Ihara, R., and Fujiwara, T. (2011). Green-emissive Mn-activated nanocrystallized glass with willemite-type Zn_2GeO_4. *Opt. Mater. Express* 1: 372–378.

68 Yu, Y., Wang, J., Wang, J. et al. (2017). Structural characterization and optical properties of longlasting $CaAl_2O_4$:Eu^{2+},Nd^{3+} phosphors synthesized by microwave-assisted chemical co-precipitation. *J. Rare Earths* 35: 652–657.

69 Chang, C.K. and Mao, D.L. (2004). Long lasting phosphorescence of $Sr_4Al_{14}O_{25}$:Eu^{2+},Dy^{3+} thin films by magnetron sputtering. *Thin Solid Films* 460: 48–52.

70 Zheng, M., Chen, X., Lei, B. et al. (2013). Synthesis and luminescence properties of flower-like $Sr_2MgSi_2O_7$:Eu^{2+},Dy^{3+} phosphor via hydrothermal-homogeneous coprecipitation route. *ECS Solid State Lett.* 2: R19–R22.

71 Lastusaari, M., Bos, A.J.J., Dorenbos, P. et al. (2015). Wavelength-sensitive energy storage in $Sr_3MgSi_2O_8$:Eu^{2+},Dy^{3+}. *J. Therm. Anal. Calorim.* 121: 29–35.

72 Yamaga, M., Ohsumi, Y., Nakayama, T., and Han, T.P.J. (2012). Persistent phosphorescence in Ce-doped Lu_2SiO_5. *Opt. Mater. Express* 2: 413–419.

73 Wang, X., Jia, J.D.D., and Yen, W.M. (2003). Mn^{2+} activated green, yellow, and red long persistent phosphors. *J. Lumin.* 102: 34–37.

74 Dai, W.B. (2014). Investigation of the luminescent properties of Ce^{3+} doped and Ce^{3+}/Mn^{2+} co-doped $CaAl_2Si_2O_8$ phosphors. *RSC Adv.* 4: 11206–11215.

75 Pang, R., Jia, Y., Zhao, L. et al. (2014). Tunable long lasting phosphorescence due to the selective energy transfer from defects to luminescent centres via tunnelling in Mn^{2+} and Tm^{3+} co-doped zinc pyrophosphate. *Dalton Trans.* 43: 9661–9668.

76 Zeng, W., Wang, Y.H., Han, S.C. et al. (2013). Design, synthesis and characterization of a novel yellow long-persistent phosphor: $Ca_2BO_3Cl:Eu^{2+},Dy^{3+}$. *J. Mater. Chem. C* 1: 3004–3011.

77 Xu, J., Ueda, J., Zhuang, Y.X. et al. (2015). $Y_3Al_{5-x}Ga_xO_{12}:Cr^{3+}$: a novel red persistent phosphor with high brightness. *Appl. Phys. Express* 8: 042602.

78 Che, G.B., Li, X.Y., Liu, C.B. et al. (2008). Long-lasting phosphorescence properties of Mn^{2+}-doped $Cd_2Ge_7O_{16}$ orange light-emitting phosphor. *Phys. Status Solidi A* 205: 194–198.

79 Wang, F., Yang, B., Liu, D.C. et al. (2014). Influence of vacuum upon preparation and luminescence of Si^{4+} and Ti^{4+} co-doped $Gd_2O_2S:Eu$ phosphor. *Spectrochim. Acta Part A* 126: 46–52.

80 Hang, T., Liu, Q., Mao, D.L., and Chang, C.K. (2008). Long lasting behavior of $Gd_2O_2S:Eu^{3+}$ phosphor synthesized by hydrothermal routine. *Mater. Chem. Phys.* 107: 142–147.

81 Li, Y.J., Wang, M.W., Zhang, L.D. et al. (2013). Soft chemical synthesis and luminescence properties of red long-lasting phosphors $Y_2O_2S:Sm^{3+}$. *Int. J. Miner. Metall. Mater.* 20: 972–977.

82 Cui, C.E., Jiang, G.W., Huang, P. et al. (2014). Synthesis and characterization of $Y_2O_2S:Eu^{3+},Mg^{2+},Ti^{4+}$ nanotubes via hydrothermal method. *J. Lumin.* 145: 665–668.

83 Jin, Y.H., Hu, Y.H., Chen, L. et al. (2013). Luminescence properties of dual-emission (UV/visible) long afterglow phosphor $SrZrO_3:Pr^{3+}$. *J. Am. Ceram. Soc.* 96: 3821–3827.

84 Noto, L.L., Pitale, S.S., Gusowki, M.A. et al. (2013). Afterglow enhancement with In^{3+} co-doping in $CaTiO_3:Pr^{3+}$ red phosphor. *Powder Technol.* 237: 141–146.

85 Boutinaud, P., Sarakha, L., and Mahiou, R. (2009). $NaNbO_3:Pr^{3+}$: a new red phosphor showing persistent luminescence. *J. Phys.:Condens. Matter* 21: 025901.

86 Liu, Z.R. and Zhong, R.X. (2013). Green and red long lasting phosphorescence (LLP) in γ-$Zn_3(PO_4)_2:Mn^{2+}/Ga^{3+}$. *J. Alloys Compd.* 556: 6–11.

87 Lei, B.F., Man, S.Q., Du, Y.L., and Yue, S. (2010). Luminescence properties of Sm^{3+}-doped $Sr_3Sn_2O_7$ phosphor. *Mater. Chem. Phys.* 124: 912–915.

88 Liu, Y., Wang, Z., Miao, K. et al. (2022). Research progress on near-infrared long persistent phosphor materials in biomedical applications. *Nanoscale Adv.* 4: 4972–4996.

89 Jia, D., Lewis, L., and Wang, X. (2010). Cr^{3+}-doped lanthanum gallogermanate phosphors with long persistent IR emission. *Electrochem. Solid-State Lett.* 13: J32–J34.

90 Kamimura, S., Xu, C., Yamada, H. et al. (2014). Long-persistent luminescence in the near-infrared from Nd^{3+}-doped Sr_2SnO_4 for in vivo optical imaging. *Jpn. J. Appl. Phys.* 53: 092403.

91 Xu, J., Murata, D., Katayama, Y. et al. (2017). Cr^{3+}/Er^{3+} co-doped $LaAlO_3$ perovskite phosphor: a near-infrared persistent luminescence probe covering the first and third biological windows. *J. Mater. Chem. B* 5: 6385–6393.

92 Liu, F., Liang, Y., Chen, Y., and Pan, Z. (2016). Divalent nickel-activated gallate-based persistent phosphors in the short-wave infrared. *Adv. Opt. Mater.* 4: 562–566.

93 Yang, Y., Wang, K.-Z., and Yan, D. (2017). Lanthanide doped coordination polymers with tunable afterglow based on phosphorescence energy transfer. *Chem. Commun.* 53: 7752–7755.

94 Parker, C.A. and Hatchard, C.G. (1961). Triplet-singlet emission in fluid solutions. Phosphorescence of eosin. *Trans. Faraday Soc.* 57: 1894–1904.

95 Endo, A., Ogasawara, M., Takahashi, A. et al. (2009). Thermally activated delayed fluorescence from Sn^{4+}–porphyrin complexes and their application to organic light emitting diodes- a novel mechanism for electroluminescence. *Adv. Mater.* 21: 4802–4806.

96 Endo, A., Sato, K., Yoshimura, K. et al. (2011). Efficient up-conversion of triplet excitons into a singlet state and its application for organic light emitting diodes. *Appl. Phys. Lett.* 98: 083302.

97 Solov, ev, K.N. and Borisevich, E.A. (2005). Intramolecular heavy-atom effect in the photophysics of organic molecules. *Phys. Usp.* 48: 231–253.

98 Dinh, T.V., Yen, E.L., and Winefordner, J.D. (1976). Heavy-atom effect on room temperature phosphorimetry. *Anal. Chem.* 48: 1186–1188.

99 Yang, S., Wu, D., Gong, W. et al. (2018). Highly efficient room-temperature phosphorescence and afterglow luminescence from common organic fluorophores in 2D hybrid perovskites. *Chem. Sci.* 9: 8975–8981.

100 Ema, K., Inomata, M., Kato, Y. et al. (2008). Nearly perfect triplet-triplet energy transfer from wannier excitons to naphthalene in organic-inorganic hybrid quantum-well materials. *Phys. Rev. Lett.* 100: 257401.

101 Yang, Y., Wang, K.-Z., and Yan, D. (2017). Smart luminescent coordination polymers toward multimode logic gates: time-resolved, tribochromic and excitation-dependent fluorescence/phosphorescence emission. *ACS Appl. Mater. Interfaces* 9: 17399–17407.

102 Mujahid, M.H., Upadhyay, T.K., Khan, F. et al. (2022). Metallic and metal oxide-derived nanohybrid as a tool for biomedical applications. *Biomed. Pharmacother.* 155: 113791.

103 Price, J., Allan, P., and Slater, P. (2023). Optimising the synthesis of $LiNiO_2$: coprecipitation versus solid-state, and the effect of molybdenum doping. *Energy Adv.* 2: 864.

104 Fernández-Arias, M., Vilas, A.M., Boutinguiza, M. et al. (2022). Palladium nanoparticles synthesized by laser ablation in liquids for antimicrobial applications. *Nanomaterials* 12 (15): 2621.

105 Barizão, A., Oliveira, J., Gonçalves, R., and Cassini, S. (2021). Nanomagnetic approach applied to microalgae biomass harvesting: advances, gaps, and perspectives. *Environ. Sci. Pollut. Res.* 28: 1–17.

106 Girija, E., Sekar, K., Duraisamy, K. et al. (2019). Synthesis of NIR emitting rare earth doped fluorapatite nanoparticles for bioimaging applications. *Curr. Phys. Chem.* 09.

107 Makkara, M. and Viswanatha, R. (2018). Frontier challenges in doping quantum dots: synthesis and characterization. *RSC Adv.* 8: 22103–22112.

108 Duraisamy, S., Ganguly, A., Sharma, P.K. et al. (2021). One-step hydrothermal synthesis of phase-engineered MoS_2/MoO_3 electrocatalysts for hydrogen evolution reaction. *ACS Appl. Nano Mater.* 4: 2642–2656.

109 Xu, J., Ueda, J., Kuroishi, K., and Tanabe, S. (2015). Fabrication of Ce^{3+}–Cr^{3+} co-doped yttrium aluminium gallium garnet transparent ceramic phosphors with super long persistent luminescence. *Scr. Mater.* 102: 47–50.

110 Gupta, S.K. and Mao, Y. (2021). A review on molten salt synthesis of metal oxide nanomaterials: status, opportunity, and challenge. *Prog. Mater. Sci.* 117: 100734.

111 Gupta, S.K. and Mao, Y. (2021). Recent developments on molten salt synthesis of inorganic nanomaterials: a review. *J. Phys. Chem. C* 125 (12): 6508–6533.

112 Nag, A. and Kutty, T.R.N. (2003). Role of B_2O_3 on the phase stability and long phosphorescence of $SrAl_2O_4$:Eu,Dy. *J. Alloys Compd.* 354 (1–2): 221–231.

113 Bierwagen, J., Delgado, T., Jiranek, G. et al. (2021). Observation of multiple sites for trivalent europium ions in $SrAl_2O_4$. *J. Lumin.* 222: 117113.

114 Carvalho, J.M., der Heggen, D.V., Martin, L.I.D.J., and Smet, P.F. (2020). Microwave-assisted synthesis followed by a reduction step: making persistent phosphors with a large storage capacity. *Dalton Trans.* 49 (14): 4518–4527.

115 Havasi, V., Tátrai, D., Szabó, G. et al. (2020). On the effects of milling and thermal regeneration on the luminescence properties of Eu^{2+} and Dy^{3+} doped strontium aluminate phosphors. *J. Lumin.* 219: 116917.

116 Relvas, M., Soares, M.R.N., Pereira, S.O. et al. (2019). Trends in Cr^{3+} red emissions from $ZnGa_2O_4$ nanostructures produced by pulsed laser ablation in a liquid medium. *J. Phys. Chem. Solids* 129: 413–423.

117 Srivastava, B.B., Kuang, A., and Mao, Y. (2015). Persistent luminescent sub-10 nm Cr doped $ZnGa_2O_4$ nanoparticles by a biphasic synthesis route. *Chem. Commun.* 51: 7372–7375.

118 Glais, E., Pellerin, M., Castaing, V. et al. (2018). Luminescence properties of $ZnGa_2O_4$:Cr^{3+},Bi^{3+} nanophosphors for thermometry applications. *RSC Adv.* 8 (73): 41767–41774.

119 Srivastava, B.B., Gupta, S.K., Mohan, S., and Mao, Y. (2021). Molten-salt-assisted annealing for making colloidal $ZnGa_2O_4$:Cr nanocrystals with high persistent luminescence. *Chem Eur J* 27 (44): 11398–11405.

120 Mondal, A. and Manam, J. (2020). Structural, optical and temperature dependent photoluminescence properties of Cr^{3+}-activated $LaGaO_3$ persistent phosphor for optical thermometry. *Ceram. Int.* 46: 23972–23984.

121 Srivastava, B.B., Gupta, S.K., and Mao, Y. (2020). Remarkable enhancement of photoluminescence and persistent luminescence of NIR emitting $ZnGa_2O_4$:Cr^{3+} nanoparticles. *CrystEngComm* 22 (14): 2491–2501.

122 Boiko, V., Dai, Z., Markowska, M. et al. (2021). Particle size-related limitations of persistent phosphors based on the doped $Y_3Al_2Ga_3O_{12}$ system. *Sci. Rep.* 11: 141.

123 Zhanga, X., Zhanga, J., Rena, X., and Wanga, X.-J. (2008). The dependence of persistent phosphorescence on annealing temperatures in $CaTiO_3:Pr^{3+}$ nanoparticles prepared by a coprecipitation technique. *J. Solid State Chem.* 181: 393–398.

124 Zhan-Jun, L., Hong-Wu, Z., Meng, S. et al. (2012). A facile and effective method to prepare long-persistent phosphorescent nanospheres and its potential application for in vivo imaging. *J. Mater. Chem.* 22: 24713–24720.

125 Li, Z., Zhang, Y., Wu, X. et al. (2015). In vivo repeatedly charging near-infrared-emitting mesoporous $SiO_2/ZnGa_2O_4:Cr^{3+}$ persistent luminescence nanocomposites. *Adv. Sci.* 2: 1500001.

126 Merízio, L.G., Lodi, T.A., Bonturim, E., and de Camargo, A.S.S. (2022). Persistent luminescent phosphor-in-glass composites based on $NaPO_3$–Ga_2O_3 glasses loaded with $Sr_2MgSi_2O_7:Eu^{2+},Dy^{3+}$. *Opt. Mater.* 134: 113046.

127 Du, J. and Poelman, D. (2020). Red-light-activated red-emitting persistent luminescence for multicycle bioimaging: a case study of CaS: Eu^{2+},Dy^{3+}. *J. Phys. Chem. C* 124 (30): 16586–16595.

128 Heggen, D.V.der., Joos, J.J., and Smet, P.F. (2018). Importance of evaluating the intensity dependency of the quantum efficiency: impact on LEDs and persistent phosphors. *ACS Photonics* 5: 4529–4537.

129 De Clercq, O.Q., Martin, L.I.D.J., Korthout, K. et al. (2017). Probing the local structure of the near-infrared emitting persistent phosphor $LiGa_5O_8:Cr^{3+}$. *J. Mater. Chem. C* 5 (41): 10861–10868.

130 Du, J., De Clercq, O.Q., and Poelman, D. (2019). Temperature dependent persistent luminescence: evaluating the optimum working temperature. *Sci. Rep.* 9 (1): 10517.

131 Gao, Q., Li, C., Liu, Y. et al. (2020). Manipulating trap filling of persistent phosphors upon illumination by using a blue light-emitting diode. *J. Mater. Chem. C* 8: 6988–6992.

132 Van der Heggen, D., Joos, J.J., Rodriguez Burbano, D.C. et al. (2017). Counting the photons: determining the absolute storage capacity of persistent phosphors. *Materials* 10 (8): 867.

133 Li, Y., Li, Y.Y., Sharafudeen, K. et al. (2014). A strategy for developing near infrared long-persistent phosphors: taking $MAlO_3:Mn^{4+},Ge^{4+}$ (M = La, Gd) as an example. *J. Mater. Chem. C* 2: 2019–2027.

134 Abdukayum, A., Chen, J.-T., Zhao, Q., and Yan, X.-P. (2013). Functional near infrared-emitting Cr^{3+}/Pr^{3+} co-doped zinc gallogermanate persistent luminescent nanoparticles with superlong afterglow for in vivo targeted bioimaging. *J. Am. Chem. Soc.* 135: 14125–14133.

135 Bessière, A., Lecointre, A., Priolkar, K., and Gourier, D. (2012). Role of crystal defects in red long-lasting phosphorescence of $CaMgSi_2O_6:Mn$ diopsides. *J. Mater. Chem.* 22: 19039–19046.

136 Zhuang, Y., Chen, D., Chen, W. et al. (2021). X-ray-charged bright persistent luminescence in $NaYF_4:Ln^{3+}@NaYF_4$ nanoparticles for multidimensional optical information storage. *Light Sci. Appl.* 10: 132.